



Supplementary Information for

Particle motion on burned and vegetated hillslopes

Danica L. Roth, Tyler H. Doane, Joshua J. Roering, David J. Furbish & Aaron Zettler-Mann

Danica L. Roth
droth@mines.edu

This PDF file includes:

Methods
Figures S1 to S2
Tables S1 to S2
Legends for Movies S1 to S2
SI References

Other supplementary materials for this manuscript include the following:

Movies S1 to S2

Methods

1. Topographic data collection, processing and analysis

Field sites were selected for maximum distances over which slopes remained approximately planar and roughness visually uniform. Point cloud data were collected for four heavily vegetated sites ($S_{veg} = 0.25, 0.36, 0.45, 0.75$) and three severely burned sites ($S_{burn} = 0.31, 0.36, 0.53$). Data for the steepest vegetated site ($S=0.81$) was collected by UNAVCO using a Riegl terrestrial lidar scanner (TLS) which also collects concurrent high-resolution digital photography that generates colorized final point clouds. TLS clouds were co-registered, range-filtered (50 m) and octree filtered (0.01 m) using RiScan software. Photogrammetric imagery was collected by hand at the remaining vegetated sites and by drone flight at all burned sites, then processed into 3D point clouds using Agisoft PhotoScan. All further point cloud processing was conducted in CloudCompare. The boundaries of each surface used in rock drop experiments were identified in point clouds using measuring tapes, reflectors and other physical markers visible in colorized point clouds, and confirmed with field photographs and notes recording measured distances to easily discernable features. Point clouds were clipped to only the experimental surfaces within these boundaries for topographic analysis.

To our knowledge, no point cloud vegetation removal algorithms exist that are equipped to deal with the density of old growth Oregon Coast Range vegetation. Due to the presence of large trees in the lidar point cloud, the steepest vegetated site was filtered to remove points with a vertical distance greater than 1 m from a coarse, approximate “bare ground” surface that was fit with a 2D quadratic (using CloudCompare’s standard 2.5D quadratic fit method, which first performs a planar fit to identify the point cloud’s ‘most flat’ dimension, i.e., with lowest variance) to the minimum point elevations within every 1 m² cell (to avoid biasing the fit by vegetation). A higher resolution “bare ground” surface and its best-fit plane were generated for every point cloud by selecting the points with minimum elevation in each 0.5-m resolution grid cell. To achieve constant point density, the original point clouds (with vegetation filtered to 1 m for the steepest vegetated site, as discussed above) were rasterized to 1 cm grids using the average elevation in each grid cell. To examine surface roughness, we then calculated the surface-normal distance $r(x, y)$ from each cell to the best-fit 0.5-m “bare ground” plane. We use surface-normal rather than vertical distances throughout this analysis as this better represents the dimension of surface roughness that acts as a barrier to particle motion, particularly on very steep slopes. Surface-normal rasters were then filtered with a gaussian ($\sigma = 1 \text{ m} = \text{kernel size}$)

in Matlab to find their low-pass (long-wavelength) surfaces, representing deviation $r_{lp}(x, y)$ about the hillslope plane over larger scales ($\gtrsim 1\text{-m spatial wavelength}$). Low-pass surfaces were then subtracted from the surface-normal rasters to produce high-pass (short-wavelength) surfaces $r_{hp}(x, y) = r(x, y) - r_{lp}(x, y)$ representing smaller-scale deviation ($\lesssim 1\text{-m spatial wavelength}$) about each low-pass surface. Example transects for each site and surface are shown in Figs. 2 and S2.

The median diameter of particles composing a given surface is a common metric for characterizing the roughness of channel beds (1, 2) and talus slopes (3). On heavily weathered, soil mantled hillslopes, however, surface topography and microtopography are more relevant than surface particle size. We therefore regard the high-pass surface deviation $r_{hp}(x, y)$ as an effective “radius” of surface roughness at each point. We calculate corresponding surface-normal roughness heights $d(x, y) = 2|r_{hp}(x, y)|$ over each experimental surface and use their median value d_{50} as a metric for roughness over scales $\lesssim 1 \text{ m}$ at each site.

We selected the approaches above as the most appropriate given the relevant processes and conventions. However, our overall results are insensitive to variation in gaussian filter parameters ($0.5 \text{ m} < \sigma < 2 \text{ m}$, kernel size $1\sigma - 5\sigma$), the area over which roughness d_{50} is computed, and regardless of whether we use vertical elevations rather than surface-normal distances, or their standard deviations (another common roughness metric (4)) rather than median values.

2. Rock drop experiments

Particles found *in situ* at our field sites were generally small, angular, composed of deeply weathered mudstone and sandstone from the local Tyee formation, and unable to survive our experiments without breaking. We therefore obtained experimental particles from Lane Forest Products, a landscape supply company in Eugene, OR. To isolate the variables of interest (slope, grain size and surface roughness), we limited our selection to particles available in three distinct size classes with similar composition and shapes. This limited our selection to rounded to subrounded particles (Figs. 1, S1, Supplemental Videos).

At each hillslope site, we measured slope-parallel travel distances for $N=100$ clasts in each of three size classes (2100 total; median intermediate diameters $D_{50} = 1.7 \text{ cm}, 4.4 \text{ cm}, \text{ and } 7.3 \text{ cm}$; see Table S1 for additional particle parameters) dropped in a random orientation and random position along a demarcated starting line from a constant height of 20 cm above the ground measured to particle centers (see Supplemental Videos). Starting position and height were marked using a string tied taut

between two pieces of rebar, which was remeasured regularly throughout experiments to assure continued accuracy at all locations along its length. To avoid altering the surface roughness of the study sites with footprints, we refrained from stepping on the experimental slopes while conducting experiments or collecting topographic data. Travel distances of $x < 1$ m were therefore measured by hand, but alternate methods were used to assess longer travel distances. On the burned slopes, travel distances of $x > 1$ m were measured with a cord held cross-slope over each particle and across a pair of slope-parallel measuring tapes framing the lateral edges of each site. On the forested slopes, distances of $x > 1$ m were measured by using a laser rangefinder with accuracy of ± 0.3 m to survey the distance (visually corroborated with slope-parallel measuring tapes) to a reflective disc held on a “Carp Gangster” pole over each particle to avoid errors due to vegetation in the laser’s line of sight.

3. Empirical travel distance distributions

The exceedance probability or likelihood of a particle traveling farther than x can be expressed as (5):

$$R(x) = e^{-\int_0^x P(x')dx'}. \quad [S1]$$

Because the particles were dropped, the initial horizontal component of particle motion depends on the initial impact with the surface and is highly variable. To exclude this variability from our analysis, we therefore truncate travel distances $x \leq 0.1$ m and recalculate travel distances from this position (i.e., set this to $x = 0$) to examine only the population of particles that travel at least a distance of 0.1 m. All empirical particle travel distances $x = \{x_1, x_2, \dots, x_N\}$ were treated as type I right-censored. A censoring distance x_{censor} was selected for each experimental setup based on slope breaks assessed in the topographic data and cross-referenced with field observations. These included both hillslope-scale slope breaks (i.e., distance at which a given hillslope ceases to be approximately planar, for example, at the base of the hill) and smaller, localized changes in slope relative to grain size (i.e., surface variation or roughness elements such as vegetation) that were manually censored in cases where they caused obvious overweighting of tail data that biased the distribution fits (Figs., 2 and S2), although the qualitative results of our analysis were robust regardless of precise censor location selection. We assume the maximum empirical cumulative travel distance probability must be < 1 even for datasets in which all measurements $x < x_{censor}$, and therefore normalize all probability distributions by $N + 1$. For each dataset, we compute an empirical cumulative

distribution function $F(x)$ using the built-in `ecdf` function in Matlab, then linearly interpolate a censored cumulative distribution $F(x_i)$ over $0 \leq x_i < x_{censor}$ at equal intervals Δx_i set to the minimum sample interval in x to avoid loss of resolution. We calculate an empirical probability density $f(x_i) = \frac{\Delta F(x_i)}{\Delta x_i}$, exceedance $R(x_i) = 1 - F(x_i)$, and disentrainment (5) $P(x_i) = \frac{f(x_i)}{R(x_i)}$ for each dataset with $\Delta F(x_i) = F(x_i) - F(x_i - \Delta x_i)$. Our final censored empirical distributions $f(x)$, $R(x)$ and $P(x)$ were cut to include only those values at original sample distances x .

4. Lomax distribution optimization

For Lomax optimization, an additional $x_{N+1} > x_{censor}$ sample was added to each right-censored travel distance dataset for $N+1$ normalization. Lomax exceedance distribution functions were fit to each dataset using Matlab’s built-in custom optimization function, `fminsearch`, to simultaneously optimize Lomax parameters A and B via least squares minimization of log deviations $\sum[\log(R) - \log(\hat{R})]^2$, between empirical exceedance $R(x)$ and model exceedance $\hat{R}(x) = (\frac{Ax}{B} + 1)^{-1/A}$. Error minimization was set to require $B > 0$ (i.e., disentrainment rates must be positive), and $-\frac{B}{A} > \max(x)$ for $A < 0$, or $-\frac{B}{A} < \min(x)$ for $A > 0$ (i.e., the asymptote of R must allow for the range of observed x -values) (Figure 4). Model exceedance values were cut if they fell below $\hat{R} = 0.001$ (estimated error tolerance threshold) or above $\hat{R} = 1$ (probability limit).

Uncertainty estimates σ_A and σ_B were obtained through a bootstrap procedure. Each $\hat{R}(A, B)$ was randomly resampled ($N_b = 100$) with replacement 1000 times. Each bootstrapped sample was then individually optimized for parameter A_b with parameter B fixed to its estimated value, and for B_b with parameter A fixed to its estimated value. We use the standard deviation σ_{A_b} and σ_{B_b} of all bootstrapped values A_b and B_b as an estimate for each parameter’s uncertainty, and propagation of uncertainty by the method of moments yields

$$\sigma_B = \sqrt{\left(\frac{B}{A^2}\sigma_{A_b}\right)^2 + \left(\frac{1}{A}\sigma_{B_b}\right)^2 - \frac{2B}{A^3}\sigma_{A_b}\sigma_{B_b}}, \quad [S2]$$

where $\sigma_{A,B}$ is the covariance of bootstrapped A_b and B_b parameters. While this approach is not precisely accurate because we optimize the bootstrapped parameters individually rather than jointly (whereas error is jointly distributed over A and B), it provides a reasonable estimate of relative parameter uncertainty.



Fig. S1. Photos of experimental surfaces and setup at burned field sites (top) with gradients **a)** $S=0.31$, **b)** $S=0.36$, and **c)** $S=0.53$; and vegetated sites (bottom) with gradients **d)** $S=0.25$, **e)** $S=0.36$, **f)** $S=0.45$, and **g)** $S=0.81$. White arrows begin approximately at experimental starting lines and indicate direction of particle motion.

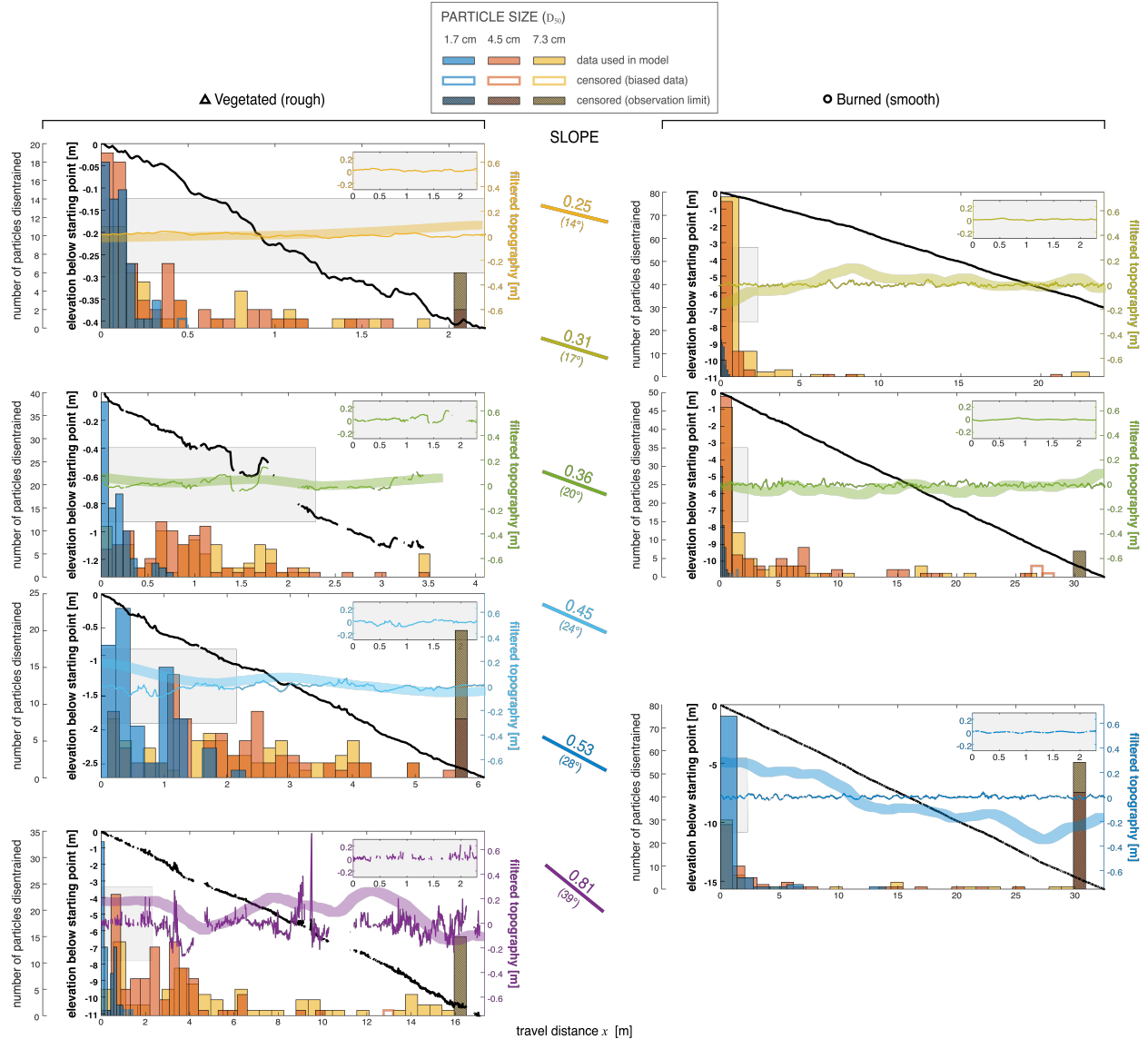


Fig. S2.

Example hillslope profiles (black lines) and particle travel distance histograms for all hillslopes. For each transect, long-wavelength gaussian filtered topography (thick colored lines) represents surface-normal variations about the mean hillslope plane over distances $\gtrsim 1$ m, while short-wavelength topography (thin colored lines) captures smaller variations about that long-wavelength surface over distances $\lesssim 1$ m. Because data for each site is shown on scaled axes for visibility, gray insets show a portion of each short-wavelength transect for comparison over the same length scale $0 < x < 2.3$, indicated by gray bars on the main figures for reference. Histograms include all recorded data, including data censored due to surpassing the limit of observations and due to biasing Lomax fits by overweighting the distribution tails (Methods).

Table S1. Experimental field site locations

	Gradient	Latitude	Longitude
Burned	0.31	42.92307 N	-123.51698 E
	0.36	42.92338 N	-123.51710 E
	0.53	42.92323 N	-123.51774 E
Vegetated	0.25	44.16599 N	-123.60432 E
	0.36	44.16595 N	-123.60398 E
	0.45	44.16596 N	-123.60400 E
	0.81	44.16607 N	-123.60420 E

Table S2. Experimental particle characteristics

Diameter (intermediate axis) (cm)	Mass (g)	Density* (g cm ⁻³)
1.7 ± 0.2	6.44 ± 2.07	3 ± 0.5
4.5 ± 0.4	105.83 ± 25.44	2.6 ± 0.20
7.2 ± 0.8	435.45 ± 97.23	2.9 ± 0.19

Mean ± standard deviation from N=25 samples of each size class.

* Density calculated from particle mass and volume (not reported) measurements.

Movie S1 (separate file).

Video of example experimental rock drop demonstrating motion dominated by sliding (particle $D_{50} \sim 7.2$ cm, $S = 0.81$).

Movie S2 (separate file).

Video of example experimental rock drop shows motion dominated by tumbling and bouncing with rotation around the shortest particle axis (particle $D_{50} \sim 7.2$ cm, $S = 0.81$).

SI References

1. J. W. Kirchner, W. E. Dietrich, F. ISEYA, H. IKEDA, The variability of critical shear stress, friction angle, and grain protrusion in water-worked sediments. *Sedimentology* **37**, 647–672 (1990).
2. G. Parker, P. C. Klingeman, On why gravel rivers are paved. *Water Resour. Res.* **18**, 1409–1423 (1982).
3. M. J. Kirkby, I. Statham, Surface Stone Movement and Scree Formation. *J. Geol.* **83**, 349–362 (1975).
4. R. A. DiBiase, M. P. Lamb, V. Ganti, A. M. Booth, Slope, grain size, and roughness controls on dry sediment transport and storage on steep hillslopes. *J. Geophys. Res. Earth Surf.* **122**, 941–960 (2017).
5. D. J. Furbish, J. J. Roering, Sediment disentrainment and the concept of local versus nonlocal transport on hillslopes. *J. Geophys. Res. Earth Surf.* **118**, 937–952 (2013).